

THE TRAIL OF DISCRETE X-RAY SOURCES  
 IN THE EARLY-TYPE GALAXY NGC 4261:  
 ANISOTROPY IN THE GLOBULAR CLUSTER DISTRIBUTION?

LEA GIORDANO<sup>1</sup>, LUCA CORTESE<sup>1,4</sup>, GINEVRA TRINCHIERI<sup>2</sup>, ANNA WOLTER<sup>2</sup>, MONICA COLPI<sup>1</sup>, GIUSEPPE GAVAZZI<sup>1</sup>, LUCIO MAYER<sup>3</sup>

*Submitted to ApJ*

ABSTRACT

*Chandra* images of the elliptical galaxy NGC 4261 have revealed an anisotropy in the spatial distribution of the off-nuclear X-ray sources, interpreted by Zezas et al. as evidence of an association with a young stellar population. Our independent analysis of archive X-ray (*Chandra*) and optical (INT and *HST*) observations confirms the anisotropy of the X-ray sources but conducts to a different interpretation for their origin. We find that nearly half of the X-ray sources are associated to a globular cluster (optical counterpart) suggesting that they are accreting low-mass X-ray binaries. Where color index information is available, the X-ray sources are found to reside in red (metal-rich) systems. The luminosity function of the X-ray sources is also consistent with the one drawn from a population of Low Mass X-ray Binaries. We further investigate the properties of the sample of point-like sources obtained from archival optical images that we suggest are good globular cluster candidates and for which we find that the projected spatial distribution is non-homogeneous. In addition, we show that the distributions of the optical and X-ray populations are very similar, which leads us to conclude that the spatial anisotropy of the X-ray sources in NGC 4261 is mostly a reflection of the anisotropy of the globular cluster population.

*Subject headings:* binaries: close — galaxies: elliptical and lenticular, cD — globular clusters: general — X-rays: binaries — X-rays: galaxies

1. INTRODUCTION

NGC 4261 is an early-type galaxy in the Virgo West Cloud, at the distance of 32 Mpc (Gavazzi et al. 1999). It belongs to a group of galaxies (Garcia 1993; Nolthenius 1993) that does not show prominent sign of gravitational interactions. The H-band luminosity of NGC 4261 is  $7.9 \times 10^{10} L_{\odot}$  corresponding to a dynamical mass of  $9.5 \times 10^{10} M_{\odot}$  (using a mass to light ratio of about 1.2, from Zibetti et al. 2002), ranking this galaxy among the most massive galaxies in Virgo. The optical spectrum is consistent with a dominant population of old stars ( $\sim 11$  Gyr, Gavazzi et al. 2002) and the light distribution is smooth with no evidence of sub-structure (Schweizer & Seitzer 1992; Colbert et al. 2001). NGC 4261 is a FRI radio galaxy (3C 270) showing two radio jets emanating from a nucleus hosting a supermassive black hole with a mass of about  $5 \times 10^8 M_{\odot}$  (Ferrarese et al. 1996) surrounded by a dusty torus and a nuclear disk (Jaffe et al. 1996; Ferrarese et al. 1996). The X-ray nuclear power from the underlying AGN has been well studied by *XMM* and *Chandra*: the X-ray luminosity is  $L_X \sim 5 \times 10^{41} \text{ erg s}^{-1}$ , and the X-ray spectrum is a power law absorbed by a column density  $N_H \sim 5 \times 10^{20} \text{ cm}^{-2}$ . The source appears to be embedded in diffuse hot gas ( $k_B T \sim 0.6 \text{ keV}$ ) and shows low amplitude, rapid variability (Chiaberge et al. 2003; Sambruna et al. 2003; Gliozzi et al. 2003).

Thanks to the high spatial resolution of *Chandra*,

Zezas et al. 2003 (ZHFM03 hereafter) have discovered the presence of about sixty bright off-nuclear X-ray sources in NGC 4261, which stand out for their large-scale anisotropic pattern. The anisotropy extends over an angle of  $\sim 4'$ , corresponding to a linear dimension of  $\sim 40 \text{ kpc}$  ( $\sim 5$  effective core radii large, since  $r_e = 4.6 \text{ kpc}$  for NGC 4261; Gavazzi et al. 2003). ZHFM03 interpret this anisotropy as evidence that the X-ray sources are associated with young stellar population, possibly formed in a recent episode of star formation triggered by some dynamical agent along tidal tails. In spite of any optical evidence of either a young population (the population in the nuclear regions is as old as 15 Gyrs; see Gavazzi et al. 2003 and Goudfrooij et al. 1994) or of recent merging events, ZHFM03 suggest a high mass binary origin for the majority of the sources, based on the significantly higher efficiency of the formation of High Mass X-ray Binaries relative to the Low Mass ones. This interpretation makes NGC 4261 a rather unique example, in clear contrast with *Chandra* observations of other early-type galaxies, where the X-ray sources are generally distributed nearly isotropically, trace the dominant (old) stellar population, and are believed to belong to the Low Mass X-ray Binary population (LMXB, e.g. Verbunt et al. 1984; Sarazin et al. 2003; Kim & Fabbiano 2004). In addition, a significant fraction ( $\sim 20\% - 70\%$ ) of these LMXBs is associated to globular clusters (GCs; Sarazin et al. 2003; Angelini et al. 2001; Kundu et al. 2002; Maccarone et al. 2003; Minniti et al. 2004), with a preference to GCs with redder color index, i.e., clusters that are more metal rich (Cote et al. 1998; Sarazin et al. 2003; West et al. 2004). In this perspective, the case of NGC 4261 stands out as a remarkable exception worth of further study.

We have therefore chosen to study its case again, in order to deepen our understanding of the the nature of the X-ray sources in external galaxies. For this rea-

<sup>1</sup> Università degli Studi di Milano Bicocca, Piazza della Scienza 3, 20126 Milano, Italy

<sup>2</sup> Osservatorio Astronomico di Brera, Via Brera 28, 20121 Milano, Italy

<sup>3</sup> Institute of Theoretical Physics, University of Zürich, Winterthurerstrasse 190, 8057 Zürich, Switzerland

<sup>4</sup> Laboratoire d'Astrophysique de Marseille, BP8, Traverse du Siphon, 13376 Marseille Cedex 12, France

son we have used archive observations of *Chandra*, of the Isaac Newton Telescope<sup>1</sup> (INT), and of the Hubble Space Telescope (*HST*) (see Table 1 for a summary of the dataset used) to search for optical counterparts of the X-ray sources, and to study their relation with the GC population of NGC 4261.

The outline of the paper is as follows. In §2 we describe the data reduction, in the X-ray and optical bands. In §3 we proceed on studying the properties of the optical point-like sources, and we cross-correlate the optical data with the X-ray data. We then derive the luminosity function of the X-ray source population. In §4 we investigate on the azimuthal anisotropy of the X-ray sources, and on that of the underlying GC candidate population. In the context of our new findings we discuss in §5 the nature of the sources and their potential in tracing the history of assembly of NGC 4261 in the Virgo cluster.

## 2. DATA REDUCTION

### 2.1. X-ray data

NGC 4261 was observed by *Chandra* (Weisskopf et al. 2000) with the ACIS-S3 CCD on 2000 May 6 for a total exposure of 37,210 s (see Table 1 for details). The data were collected in 1/2 sub-array mode to avoid the pile-up of the central AGN source. The active field of view is shown in Figure 1 over-plotted on an optical image of the galaxy. The data reduction was performed with the package **CIAO**<sup>2</sup> v. 3.0.2 and **CALDB** v. 2.2. Data were cleaned for high background periods due to particle induced flares and the resulting exposure time is of 28.3 ks. Individual sources were detected using a wavelet-detection algorithm (*wavdetect* in **CIAO**), with the same parameters used by ZHFM03, in three energy bands: full band (0.3 – 7.0 keV), soft band (0.3 – 2.0 keV) and hard band (2.0 – 7.0 keV). The catalog that we obtained includes 54 sources detected above the probability threshold of  $10^{-6}$  that implies  $\leq 1$  false detection due to statistical fluctuations. The positions of the X-ray sources are shown in Figure 2. In Table 2 we give the source number (column 1), the right ascension and declination J2000 (column 2 and 3). Count rates (column 4) are converted into unabsorbed luminosities (0.2 – 10 keV) assuming a power-law model with photon index 1.7 and a Galactic line of sight column density of  $N_H = 5.8 \times 10^{20} \text{ cm}^{-2}$  (Stark et al. 1992). ZHFM03 do not publish a catalog of their X-ray sources, so a comparison of the two source lists is not possible. However, a visual inspection of their Figure 1 indicate consistency. The *Chandra* data relative to the central region of this galaxy has also been analyzed by Chiaberge et al. (2003) and Gliozzi et al. (2003), who have mostly focused on the AGN emission in the X-ray, radio and optical bands.

In particular Gliozzi et al. (2003) detect 5 off-nuclear sources: A, B, C, E coincide with our sources 38, 33, 31, and 14 respectively, and D, which we do not detect (our source 19 is the closest, at  $\sim 10''$ ). Although these authors comment of the fact that they do not find optical counterparts for any of their sources, they do not comment on the possible connection of these sources with the

<sup>1</sup> Roque de Los Muchachos Observatory, La Palma, Spain (<http://www.ing.iac.es/>)

<sup>2</sup> *Chandra* Interactive Analysis of Observations (CIAO), <http://cxc.harvard.edu/ciao/>

jet, in spite of the evidence that two of them, (A and E) are aligned and at opposite ends of it.

### 2.2. Optical data

We have used archive observations of INT and *HST* WFPC2 for a systematic search of the optical counterparts of the X-ray sources.

We extracted a deep  $r'$  band image from the INT-Wide Field Camera (WFC) archive, consisting of three exposures of 500 seconds each, for a total integration time of 1500 seconds. The image covers the whole galaxy (the field of view of the INT WFC is of about  $0.5 \text{ deg}^2$ ) and has a mean seeing of  $\sim 1''$  (Khosroshahi et al. 2004). The reduction of the images was carried out using standard tasks in the **IRAF** package<sup>3</sup>. Bias subtraction and flat-field normalization were applied to each exposure using the median of several bias frames and flat-field exposures obtained during the observations. The three exposures were combined using a median filter, that automatically removes cosmic rays. Using reference catalogues of astrometric stars, we obtained a WCS solution for the whole field having a mean RMS of  $\sim 1 \text{ arcsec}$ .

*HST* WFPC2 observations cover the central portion of the galaxy, as shown by the white boxes in Figure 1. The south-east (SE) field was observed using three different filters: F675W, F547M, F791W while only the F702W filter is available for the north-west (NW) field. The exposure times of the four images are given in Table 1.

For our analysis we started from pipelined processed data. For both *HST* WFPC2 and INT, we first fitted ellipses to the isophote of the galaxy using the task **ELLIPSE** from the **IRAF** package, and subtracted the model from the data. The resulting image was then used to detect sources with **SExtractor** (Bertin & Arnouts 1996). The last isophote has a major and minor axis of 4.5 and 3.2 arcmin respectively. We improve the relative *HST* astrometry from  $\sim 0.7$  to  $\sim 0.2 \text{ arcsec}$  comparing the overlap region between the NW and SE field. On the contrary we did not try to make any improvement in the relative astrometry between *Chandra* and INT/*HST* images. We note that, for both *HST* and INT images, the model subtraction leaves a quadrupole structure in the central region. Although this region is smaller in the *HST* data, we exclude a wider area of  $\sim 0.5$  square arcmin, due to the presence of residuals in the INT data that could induce spurious results in our comparisons. This structure was already noticed by Colbert et al. (2001) for this object, and was attributed to the boxyness of the galaxy.

Using **SExtractor** we extracted point-like objects from the model subtracted images of both INT and *HST* datasets. We set a **SExtractor** detection threshold of  $2.5 \sigma$  over the local background. We select as point-like sources objects with the following properties: (i) a magnitude error smaller than 0.1, (ii) ellipticity smaller than 0.5, (iii) FWHM between 1 and 4 pixels ( $0.1\text{-}0.4 \text{ arcsec}$ ) for *HST*, as suggested by Gebhardt & Kissler-Patig

<sup>3</sup> *IRAF* is the Image Analysis and Reduction Facility made available to the astronomical community by the National Optical Astronomy Observatories, which are operated by AURA, Inc., under contract with the U.S. National Science Foundation. STSDAS is distributed by the Space Telescope Science Institute, which is operated by the Association of Universities for Research in Astronomy (AURA), Inc., under NASA contract NAS 5-26555.

(1999), and FWHM between 3 and 10 pixels (1-3 arcsec) for INT. Note that for the *HST*-SE field we based our selection upon the F675W filter owing to its longer exposure. As a final step, we have checked the SExtractor results by visual inspection, and we have removed objects on or close to the CCDs edges for the *HST* images.

### 3. RESULTS

#### 3.1. Selection of candidate globular clusters

For the SE field of the *HST* observation, we have been able to estimate the color of the sources presented in §2.2. The instrumental magnitudes, provided by SExtractor, were converted in the Johnson-Cousin V, R and I systems using the synthetic transformations given in Holtzman et al. 1995. In order to estimate the photometric error due to model subtraction we measured the photometry on the unsubtracted image using local background and apertures from the subtracted image. The difference in the V-I color of each globular cluster obtained from the two different estimates is shown in Figure 3. The distribution appears fairly gaussian with a mean difference of  $-0.003 \pm 0.07$  mag (see Figure 3). The total photometric uncertainty is thus given by the combination of the error on the measure of GCs magnitudes (given by SExtractor), the error on the zero-point (taken from Holtzman et al. 1995) and the uncertainty due to the model subtraction (0.07 mag, Fig.3). This results in a mean error on the V-I color of  $\sim 0.11$  mag. We used F547M and F791W filters to determine the color index (V-I) of the extracted objects. We select 325 objects detected in each of the three filters with V-I color between 0 and 2 (Gebhardt & Kissler-Patig 1999), that we consider GC. Their color index and magnitude distributions shown in Figure 4 are consistent with those of the globular cluster populations observed in other massive early-type galaxies (Ashman & Zepf 1998; Cote et al. 1998; Kundu & Whitmore 2001; Larsen et al. 2001; West et al. 2004), reinforcing our definition. The color index distribution spreads from  $V-I \sim 0.5$  to  $\sim 2$ , indicating that both populations of GC (red and blue) are present. Thus the unimodal distribution observed in the V-I color histogram is probably due to the blending of different GCs populations.

Since the color information is restricted to the *HST*-SE field, we cannot classify as GCs the sources extracted from the other optical images at the same confidence. However, we have first considered sources in the region common to all three datasets ( $\sim 1$  arcmin $^2$ ). The cross-correlation between the three lists indicates that  $\sim 97\%$  (37/38) and  $\sim 83\%$  (49/59) of the sources in the *HST*-NW and INT field respectively coincide with a GC in the *HST*-SE field. Given this high fraction, we are confident that even the point-like sources from the INT dataset are good “GC candidates”, in spite of the lower resolution of the instrument. In what follows, we will use the “GC candidate” list (from the INT observation), that provides an homogeneous set of optical sources over the whole galaxy.

As a final check, we have also compared the sky projected distribution of the INT and *HST* GC candidates. Since *HST*-SE and *HST*-NW fields have different exposure times, we restrict the *HST* sample to a magnitude  $R = 24.5$  (i.e. the magnitude limit of the shallowest field). The comparison is done through an adaptive ker-

nel density analysis. This technique is a two-step procedure which first applies a pilot smoothing to estimate the local density of GCs, starting from the list of their positions only, and then uses a smoothing window variable in size that decreases with increasing local density. In this way the statistical noise in low-density regions can be reduced without smearing out the high density peaks (Silverman 1986). As shown in Figure 5, the iso-density contours from the adaptive kernel analysis are in very good agreement, confirming the reliability of the INT GCs dataset. What is apparent in the figure is the peculiar distribution of the GC population, that shows two main concentrations NE and SW of the nuclear region. The presence of the same structures in both datasets ensures that it is not a feature derived from the poor subtraction in the central region (the black area in Figure 5) since the equivalent area in the *HST* data is negligible.

#### 3.2. Cross-correlation of X-Ray and Optical data

In order to investigate the nature of the X-ray sources we have looked for optical counterparts. The central source (n. 29) is identified with the AGN (Chiaberge et al. 2003; Sambruna et al. 2003; Gliozzi et al. 2003), and sources no. 27, 43 and 53 with background/foreground galaxies. The positions of the remaining X-ray sources have been cross-correlated with the GC sample, from the *HST* fields, with a matching radius of 0.5 arcsec, and from the INT dataset, with a matching radius of 1 arcsec. These choices take into account only the intrinsic astrometric uncertainties of the three datasets (see sections 2.1 and 2.2) and not the relative uncertainties eventually present between the optical and X-ray observations. Source 54 falls outside the model subtracted area, while sources no. 19, 31 and 33 fall in the central region excluded from our previous analysis. We found an optical counterpart for 23 of the 46 discrete X-ray sources that we assume all belonging to NGC 4261. The identification is indicated in Table 2. To calculate the chance coincidence probability we performed 1000 Monte-Carlo simulations by shifting the positions of the INT and *HST* optical samples by a random offset and performing again the cross-correlation. We adopted a shift larger than the search radius but small enough so the sources do not fall outside the distribution of the X-ray sources ( $\sim 1.5$  arcmin). The probability of finding more than one spurious association is  $\sim 2.5\%$  and  $\sim 0.1\%$  in the INT and *HST* sample, respectively. In Figure 6 we give a few examples that show the positions of the X-ray sources over-plotted onto the *HST* SE, *HST* NW and INT fields. The figure also demonstrates the good correspondence between the *HST* and INT counterparts, indicating again that the identifications obtained in the INT field not covered by *HST* are not severely hampered by the lower resolution of the INT image. Note that, where the color information is available, we found that all the X-ray sources inhabit a red (color index  $V-I > 1$ ) GC, see Figure 4. The optical identification with GC candidates for  $\sim 50\%$  of the X-ray sources suggests a LMXB origin for them (Verbunt & Lewin 2004).

#### 3.3. Luminosity Function of X-ray sources

We verified the above statement by comparing the cumulative X-ray luminosity function (XLF) of our sources with those derived from observations of other galaxies

(Figure 7). In particular, we use the functional forms derived by Grimm et al. (2003) and Gilfanov (2004) considered by these authors as a signature of a universal behavior for the HMXB and the LMXB populations, respectively; namely a single power-law for HMXB, with slope of  $\alpha = -0.61$ , and a broken power-law for LMXB, with slopes of  $\alpha_1 = -0.8$ , and  $\alpha_2 = -4$  for the high luminosity end<sup>4</sup>. In testing the consistency with these universal functions, we have derived the XLF using all sources in Table 2, except for the AGN (source no. 29) and the 3 interlopers (sources no. 27, 43 and 53). We performed a log-log maximum likelihood fitting procedure for both HMXB and LMXB functional forms assuming fixed slopes. We considered as free parameter the normalization factors and, in the case of a broken power law, the luminosity of the break. The resulting XLFs are shown in Figure 7. It is unquestionable that a single power-law cannot reproduce the LF of the sources in NGC 4261. It is also apparent that the LMXB broken-power law is a good representation of the data given also the value of the break luminosity, that we have left as a free parameter in the fitting procedure, and that is consistent with the Gilfanov value of  $L_b = 5.1 \cdot 10^{38} \text{ erg s}^{-1}$ . This result is consistent with the hypothesis that the X-ray sources in this galaxy are associated to a population of LMXBs. Note that we do not take into account incompleteness at low luminosities (Kim & Fabbiano 2004); however, we point out that at least at the high luminosity end (where incompleteness should not significantly affect the XLF slope) the luminosity function is much steeper than the XLF of the HMXBs.

#### 4. AZIMUTHAL ANISOTROPY IN THE GLOBULAR CLUSTER DISTRIBUTION

ZHFM03 have shown with a Kolmogorov-Smirnov test that the spatial distribution of the X-ray sources in NGC 4261 is anisotropic. Using our list of 50 sources (sources n. 29, 27, 43 and 53 excluded) we confirm the spatial anisotropy over a scale of about  $4'$  with very high confidence ( $P > 99.9\%$  from the Kolmogorov-Smirnov test). In the preceding sections we have shown that the properties of the X-ray sources in NGC 4261 are consistent with a population of LMXBs. This however does not explain yet their spatial anisotropy, which is in stark contrast with the smooth isophotal distribution of the optical light. Given the close association with the GC population, which we find also has a peculiar distribution, we have considered the possibility that the anisotropy is nothing but a manifestation of an anisotropy seeded in the GC population. In order to test this hypothesis we have first done a statistical analysis on the spatial distribution of the GC candidates.

In order to investigate both the details of the spatial distributions of the X-ray and optical sources separately and their relation we have compared the normalized surface density of sources again with an adaptive kernel density analysis on the two sets of sources. In Figure 8 we show the iso-intensity contours extracted from the kernel analysis on the GC candidate sample (thin line) and on the X-ray sources (thick line). With this figure as a guide, we have defined 6 regions (see Figure 9, right panel) in which we have simply computed the surface number den-

sity of sources for both GCs and X-ray sources, which plot in Figure 9 (left panel) as a function of the region number. The errors associated with each entry reflects the total number of sources in the region, and gives a direct measure of the significance of the observed region-to-region variations. We also test the correlation between the two datasets using the IRAF task `CROSSCOR` and we find that the highest correlation between the two datasets is consistent with a null shift.

#### 5. DISCUSSION AND CONCLUSIONS

Our combined analysis of the X-ray and optical material available for NGC 4261 shows that the large majority of the X-ray sources in NGC 4261 are accreting LMXBs. About 50% of these sources have an optical counterpart, that we identify with a GC. Where color information is available, the sources are associated with the red (metal-rich) population, as already observed in several other galaxies. Further evidence of a LMXB origin comes from the interpretation of the luminosity function, consistent with the “universal” distribution proposed by Gilfanov (2004).

The photometric analysis of the GC population of NGC 4261 carried on a portion of the galaxy (*HST*-SE field) shows that the properties of the GCs are similar to those observed in other early-type galaxies (Cote et al. 1998; Gebhardt & Kissler-Patig 1999; West et al. 2004). Furthermore this similarity extends to the connection between X-ray sources and GC population (Sarazin et al. 2003). In particular we note that the X-ray sources are preferentially associated with the brightest and reddest GCs. As in other ellipticals, we find that the GCs hosting a X-ray source are  $\sim 7\%$  and that the X-ray sources associated with GCs are  $\sim 50\%$ , consistent with the result of Kundu et al. 2002. It is therefore not surprising that NGC 4261 ranks among those galaxies having a sizable fraction of X-ray sources in GCs. The peculiarity of NGC 4261 resides mainly in the large scale anisotropy of the X-ray sources. Our adaptive kernel density analysis has highlighted the presence of a peculiar spatial distribution in the GC candidate population, and the existence of a correlation between the spatial anisotropy of the X-ray sources and the main over-densities seeded in the GC system. To our knowledge, this is the first time that X-ray sources indicate the presence of substructures in the distribution of GC.

A non uniform spatial distribution of the GC system of NGC 4261 may reflect a peculiar history of formation of this galaxy. In the paradigm of hierarchical clustering cosmogony, elliptical galaxies may be the end result of binary or multiple major mergers among gas-rich progenitors. Major mergers likely redistribute the original GC systems of the progenitor galaxies and trigger the formation of new GCs in the center as well as along the tidal tails of the new object arising from the merger. This would result in the coexistence of two populations, metal rich and metal poor clusters, that have different photometric properties, spatial distribution and dynamical characteristics, as shown in a recent work by Li et al. (2004). Hierarchical build-up also implies a second way by which galaxy can grow, namely accretion of dwarf satellites that would lose their GCs to the primary system. GCs coming from shredded satellites could also contribute to spatial anisotropies and would be mostly

<sup>4</sup> These values are taken from Table 3 of Gilfanov (2004).

metal-poor if such satellites are similar to nearby dwarfs. Evidence that either of these two mechanisms can account for a large fraction of the GC systems in ellipticals is still lacking (Strader et al. 2004). A close inspection of the photometric and kinematical properties of the GCs can in principle help disentangle many aspects of such complex galaxy genesis. NGC 4261 could be an excellent target for further investigations: combined Chandra and HST observations can thus potentially shed light on how early-type galaxies were assembled. In parallel, we are undertaking a theoretical study running high-resolution simulations of galaxy mergers similar to those carried on

in Kazantzidis et al. 2004, including a GC formation algorithm.

We thank the anonymous Referee for useful comments that helped us to improve the paper. We thank Marco Scodeggio for providing us the implementation of the algorithm used for the adaptive kernel density analysis, and Michele Bellazzini for sharp comments and suggestions. This work was supported by the Italian Ministry of University and Research (MIUR) under the national program Prin 2003.

## REFERENCES

Angelini L., Loewenstein M., Mushotzky R.F., 2001, ApJ, 557, L35  
 Ashman K.M., Zepf S.E., 1998, The Observatory, 118, 387  
 Bertin E., Arnouts S., 1996, A&AS, 117, 393  
 Chiaberge M., Gilli R., Macchetto F.D., Sparks W.B., Capetti A., 2003, ApJ, 582, 645  
 Colbert J.W., Mulchaey J.S., Zabludoff A.I., 2001, AJ, 121, 808  
 Cote P., Marzke R.O., West M.J., 1998, ApJ, 501, 554  
 Ferrarese L., Ford H.C., Jaffe W., 1996, ApJ, 470, 444  
 Garcia A.M., 1993, A&AS, 100, 47  
 Gavazzi G., Boselli A., Scodeggio M., Pierini D., Belsole E., 1999, MNRAS, 304, 595  
 Gavazzi G., Bonfanti C., Sanvito G., Boselli A., Scodeggio M., 2002, ApJ, 576, 135  
 Gavazzi G., Boselli A., Donati A., Franzetti P., Scodeggio M., 2003, A&A, 400, 451  
 Gebhardt K., Kissler-Patig M., 1999, AJ, 118, 1526  
 Gehrels N., 1996, ApJ, 303, 336  
 Gilfanov M., 2004, MNRAS, 349, 146  
 Gliozzi M., Sambruna R.M., Brandt W.N., 2003, A&A, 408, 949  
 Goudfrooij P., Hansen L., Jorgensen H.E., Norgaard-Nielsen H.U., 1994, A&AS, 105, 341  
 Grimm H.J., Gilfanov M., Sunyaev R., 2003, MNRAS, 339, 793  
 Holtzman J.A., Burrows C.J., Casertano S., et al., 1995, PASP, 107, 1065  
 Jaffe W., Ford H., Ferrarese L., van den Bosch F., O'Connell R.W., 1996, ApJ, 460, 214  
 Kazantzidis S., Mayer L., Colpi M., et al., 2005, ApJ, 623, L67  
 Khosroshahi H.G., Raychaudhury S., Ponman T.J., Miles T.A., Forbes D.A., 2004, MNRAS, 349, 527  
 Kim D., Fabbiano G., 2004, ApJ, 611, 846  
 Kundu A., Whitmore B.C., 2001, AJ, 122, 1251  
 Kundu A., Maccarone T.J., Zepf S.E., 2002, ApJ, 574, L5  
 Larsen S.S., Brodie J.P., Huchra J.P., Forbes D.A., Grillmair C.J., 2001, AJ, 121, 2974  
 Li Y., Mac Low M., Klessen R.S., 2004, ApJ, 614, L29  
 Maccarone T.J., Kundu A., Zepf S.E., 2003, ApJ, 586, 814  
 Minniti D., Rejkuba M., Funes S.J., Akiyama S., 2004, ApJ, 600, 716  
 Nolthenius R., 1993, ApJS, 85, 1  
 Sambruna R.M., Gliozzi M., Eracleous M., Brandt W.N., Mushotzky R., 2003, ApJ, 586, L37  
 Sarazin C.L., Kundu A., Irwin J.A., et al., 2003, ApJ, 595, 743  
 Schweizer F., Seitzer P., 1992, AJ, 104, 1039  
 Silverman B.W., 1986, Density estimation for statistics and data analysis, Monographs on Statistics and Applied Probability, London: Chapman and Hall, 1986  
 Stark A.A., Gammie C.F., Wilson R.W., et al., 1992, ApJS, 79, 77  
 Strader J., Brodie J.P., Forbes D.A., 2004, AJ, 127, 3431  
 Verbunt F., Lewin W.H.G., 2004, ArXiv Astrophysics e-prints  
 Verbunt F., Elson R., van Paradijs J., 1984, MNRAS, 210, 899  
 Weisskopf M.C., Tananbaum H.D., Van Speybroeck L.P., O'Dell S.L., Jul. 2000, In: Proc. SPIE Vol. 4012, p. 2-16, X-Ray Optics, Instruments, and Missions III, Joachim E. Truemper; Bernd Aschenbach; Eds., 2-16  
 West M.J., Côté P., Marzke R.O., Jordán A., 2004, Nature, 427, 31  
 Zezas A., Hernquist L., Fabbiano G., Miller J., 2003, ApJ, 599, L73  
 Zibetti S., Gavazzi G., Scodeggio M., Franzetti P., Boselli A., 2002, ApJ, 579, 261

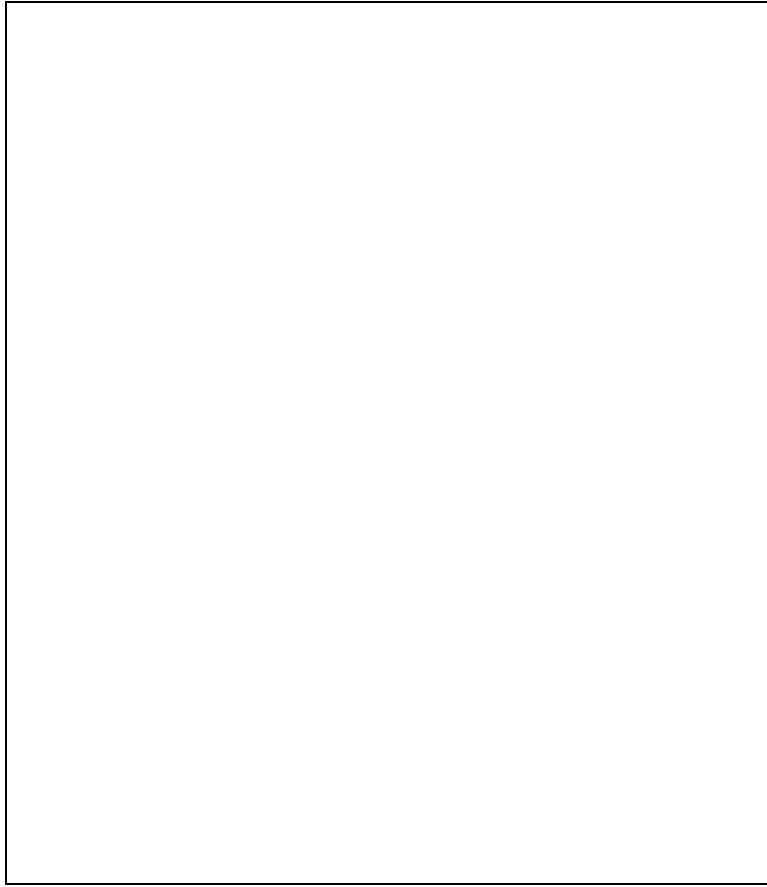


FIG. 1.— R band image of NGC 4261 from the INT telescope. The active field of the *Chandra* ACIS-S3 CCD and *HST* WFPC2 fields are superposed in black and white, respectively.

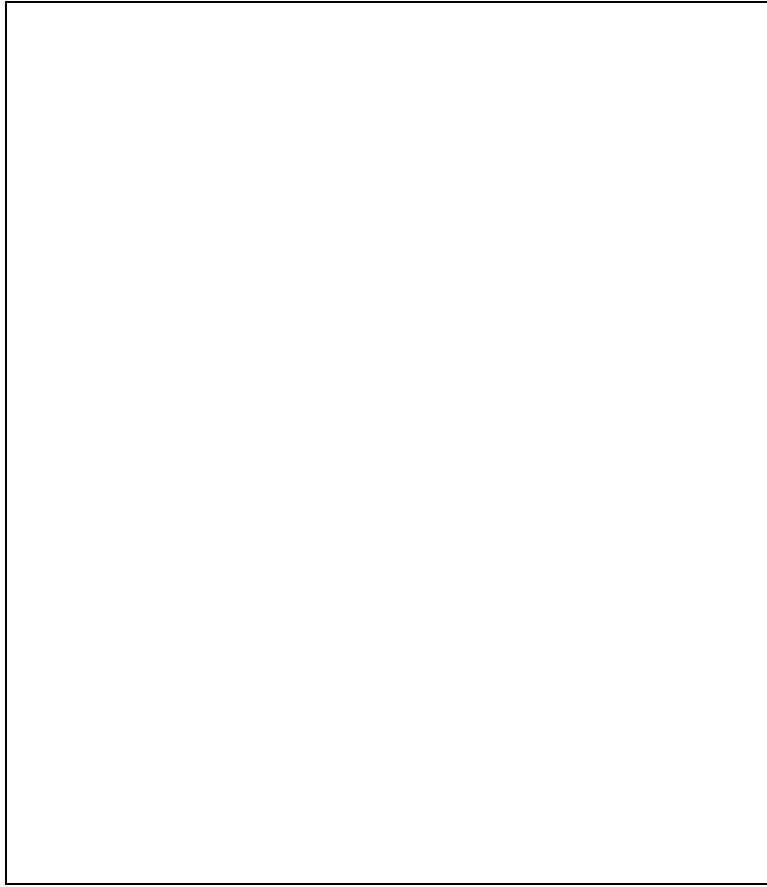


FIG. 2.— *Chandra* S3 image of NGC 4261. Open squares correspond to X-ray sources with optical counterpart while open circles to sources without optical counterpart. Excluded from the analysis are the X-ray sources (diamonds) that fall in the region where the model subtraction is too noisy, and source no. 54 located outside the galaxy radius. The black cross corresponds to the AGN. “Plus” symbols correspond to background/foreground galaxies.

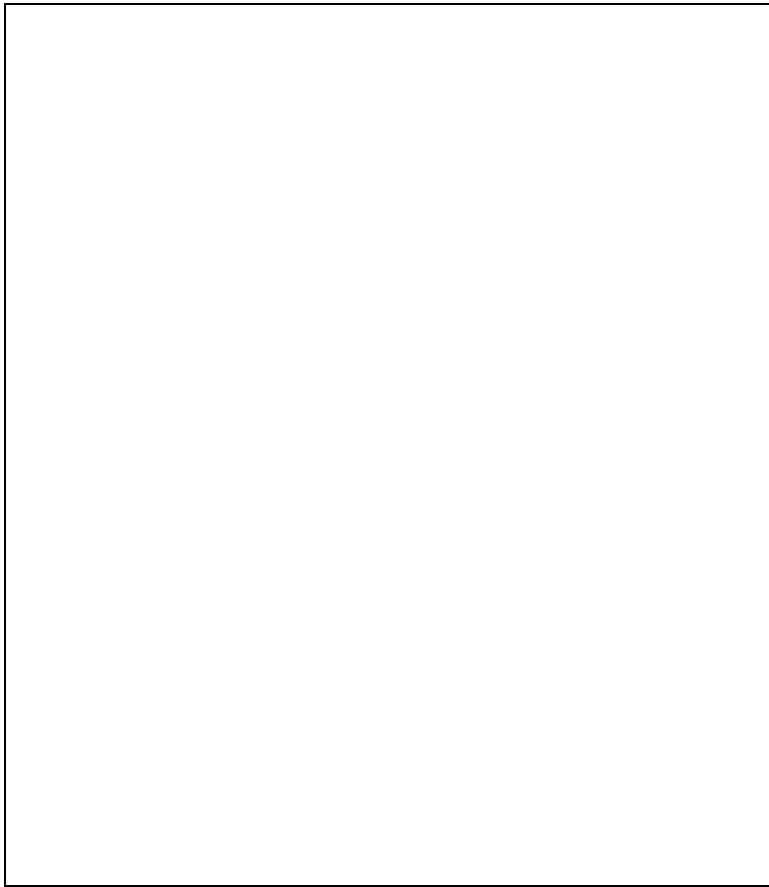


FIG. 3.— Histogram showing the difference in the estimate of the V-I color between unsubtracted and model subtracted HST images. The distribution of the GCs hosting an X-ray source is indicated in black.

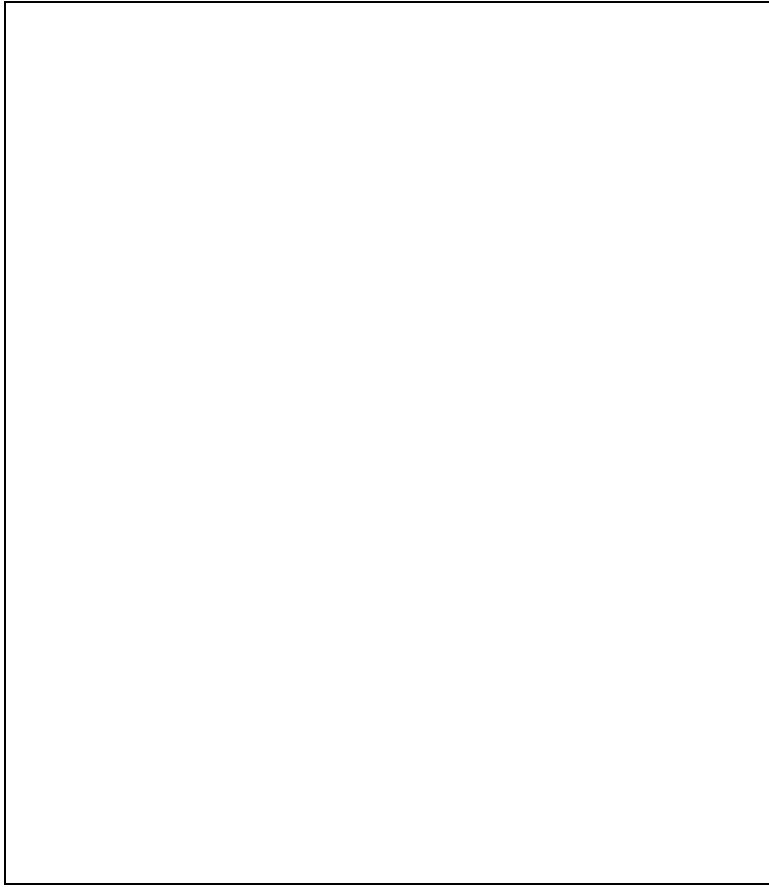


FIG. 4.— Left panel: Color index histogram of GCs in *HST* SE field. Right panel: Magnitude histogram for the GCs in *HST* SE field. In both panels the distributions of the GCs hosting an X-ray source are superposed in grey. Note that the X-ray sources inhabit preferentially metal rich (red), brighter GCs.

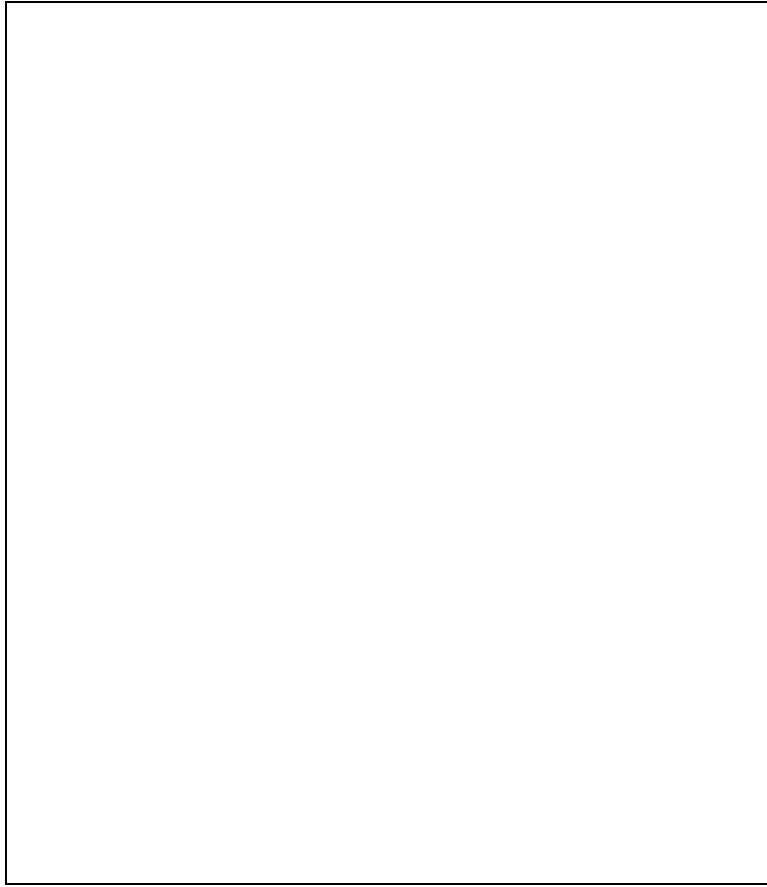


FIG. 5.— Adaptive kernel density analysis: Iso-density contours (thin line) of the analysis carried on the sample of GC candidates from INT are superposed to the iso-density contours (thick line) of the GC sample for *HST* fields. The first contour represents the  $2\sigma$  level. Black and white regions are excluded from the extraction of the optical sources. The two main overdensities coincide spatially in both data sets.

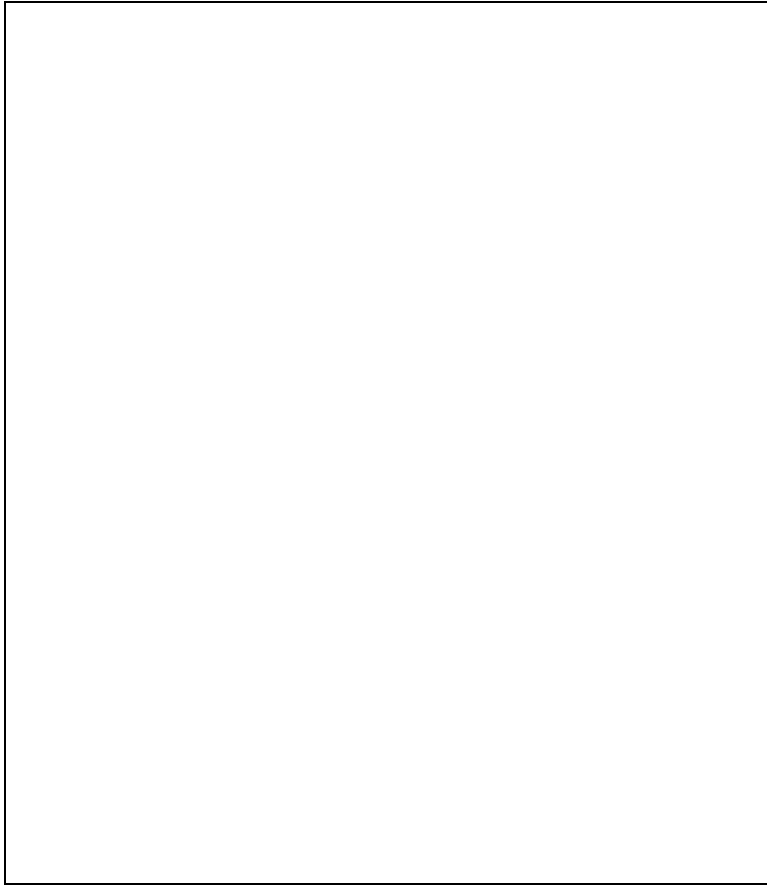


FIG. 6.— Selected X-ray sources listed in Table 2 and indicated with a star in column 1. The underlying images are from the *HST* SE (left), *HST* NW (middle) and INT (right) fields, respectively. Black circles (of radius equal to 0.7 arcsec for *HST* and 1 arcsec for INT) indicate the combined astrometric uncertainties in the position of each *Chandra* source.

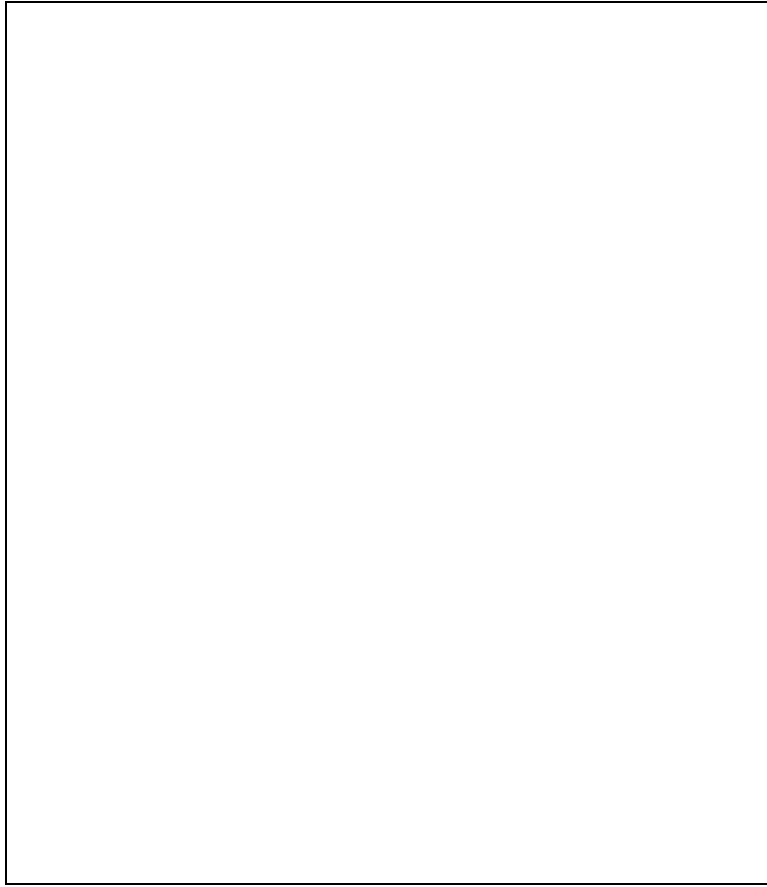


FIG. 7.— The integral luminosity function in the 0.2-10 keV band of the X-ray sources in NGC 4261. The solid line gives a broken power-law with fixed slopes, from Gilfanov (2004), renormalized to our data. We overlay the single power-law (dashed line) with a slope  $\alpha_3 = -0.61$  as suggested by Grimm et al. (2003) to describe a population of HMXBs.

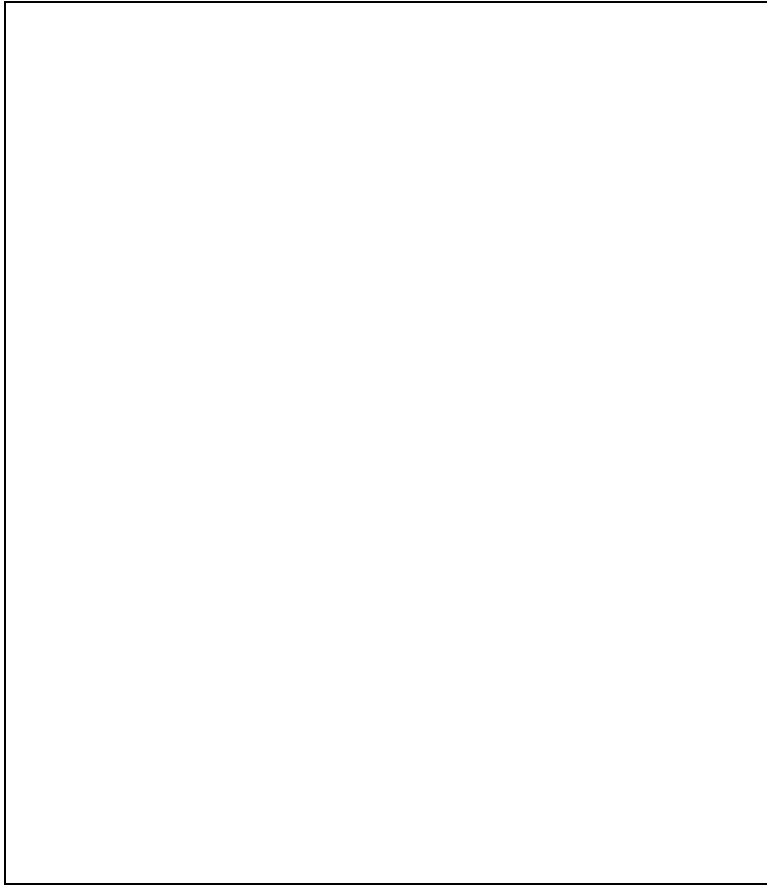


FIG. 8.— Iso-density contours from our adaptive kernel density analysis on the GC candidates from INT (thin line) and on the X-ray sources (thick line). The first contour represents the  $2\sigma$  level. Note that the main over-densities in the distribution of X-ray sources coincide with those of GC candidates.

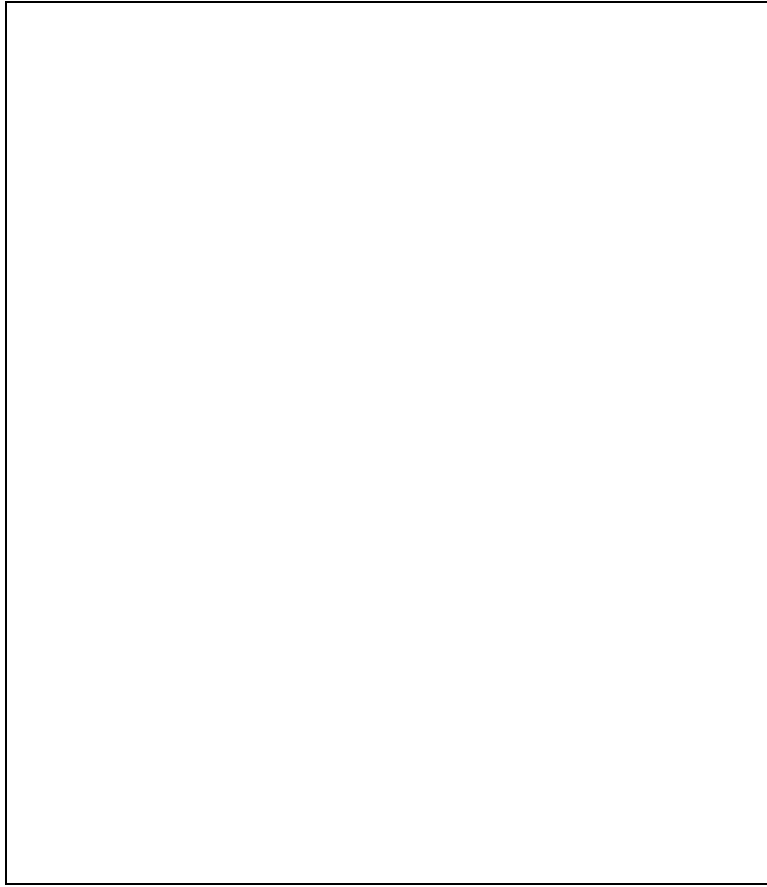


FIG. 9.— Left panel: Histogram of the surface number density (number of objects per square arcmin) of GC candidates (solid line) and of X-ray sources (dashed) as a function of their position in the field. Error bars are  $\pm 1\sigma$  computed according to Gehrels (1986). Right panel: The regions corresponding to each bin are indicated by squares superposed to the INT-model subtracted image.

TABLE 1  
JOURNAL OF ALL OBSERVATIONS USED IN THIS WORK. SMAG INDICATES THE CORRESPONDENT JOHNSON-COUSIN FILTER.

Observation	P.I.	date	instrument	filters	SMAG	exposure time (s)
optical	Ford	13 Dec 1995	<i>HST</i>	F675W	<i>R</i>	2000
optical	Ford	13 Dec 1995	<i>HST</i>	F547M	<i>V</i>	800
optical	Ford	13 Dec 1995	<i>HST</i>	F791W	<i>I</i>	800
optical	Sparks	04 May 1995	<i>HST</i>	F702W	<i>R</i>	280
optical	Osmond	04 – 10 Feb 2000	INT	<i>r'</i>	<i>R</i>	1500
X-ray	Birkingshaw	06 May 2000	<i>Chandra</i>	none	–	37210

TABLE 2

LIST OF SOURCES DETECTED IN THE FIELD OF NG C4261. COUNT RATES ARE IN THE FULL 0.3-7.0 keV BAND AS GIVEN BY *wavdetect*. X-RAY LUMINOSITIES ARE CALCULATED ASSUMING A POWER-LAW SPECTRUM WITH AN INDEX OF 1.7 AND A DISTANCE OF 32 MPC. CPT INDICATES THE ASSOCIATION WITH A GLOBULAR CLUSTER (GC) IN THE HST FIELD, A CANDIDATE GLOBULAR CLUSTER (GCC) FROM THE INT LIST, OR THE NAME OF THE FOREGROUND/BACKGROUND GALAXY. THE QUESTION MARK INDICATES THAT NO OPTICAL COVERAGE IS AVAILABLE.

source number	R.A. (h m s)	Dec (h m s)	CountRate ( $\times 10^{-4} \text{s}^{-1}$ )	$L_X(0.2 - 10 \text{keV})$ ( $\times 10^{38} \text{s}^{-1}$ )	CPT
1	12 : 19 : 14.44	+05 : 48 : 48.12	3.76 $\pm$ 1.22	4.93	...
2*	12 : 19 : 16.81	+05 : 49 : 50.43	10.65 $\pm$ 1.97	13.96	GCC
3	12 : 19 : 18.04	+05 : 49 : 54.14	2.68 $\pm$ 0.10	3.52	GCC
4	12 : 19 : 18.23	+05 : 49 : 12.10	2.03 $\pm$ 0.89	2.67	...
5	12 : 19 : 18.67	+05 : 47 : 43.23	4.15 $\pm$ 1.22	5.45	...
6	12 : 19 : 19.18	+05 : 48 : 49.31	2.63 $\pm$ 0.10	3.45	GCC
7	12 : 19 : 19.33	+05 : 49 : 06.53	2.02 $\pm$ 0.87	2.65	...
8	12 : 19 : 19.78	+05 : 48 : 22.33	4.03 $\pm$ 1.22	5.28	...
9	12 : 19 : 19.91	+05 : 48 : 50.90	4.21 $\pm$ 1.22	5.52	...
10	12 : 19 : 20.27	+05 : 49 : 08.58	7.88 $\pm$ 1.69	10.33	GCC
11	12 : 19 : 20.44	+05 : 48 : 02.72	5.18 $\pm$ 1.37	6.79	...
12	12 : 19 : 20.60	+05 : 48 : 35.89	4.97 $\pm$ 1.37	6.52	GC
13	12 : 19 : 20.66	+05 : 49 : 29.10	2.73 $\pm$ 0.10	3.58	GCC
14	12 : 19 : 20.93	+05 : 49 : 27.09	5.83 $\pm$ 1.46	7.64	GCC
15	12 : 19 : 21.00	+05 : 48 : 44.07	3.98 $\pm$ 1.22	5.22	GC
16	12 : 19 : 21.07	+05 : 50 : 17.38	3.26 $\pm$ 1.12	4.27	...
17	12 : 19 : 21.08	+05 : 48 : 07.21	2.36 $\pm$ 0.94	3.09	...
18	12 : 19 : 21.20	+05 : 47 : 52.14	5.55 $\pm$ 1.46	7.27	GCC
19	12 : 19 : 22.00	+05 : 49 : 47.02	3.43 $\pm$ 1.12	4.50	?
20	12 : 19 : 22.16	+05 : 50 : 59.57	3.07 $\pm$ 1.06	4.02	...
21	12 : 19 : 22.35	+05 : 48 : 47.95	4.27 $\pm$ 1.27	5.60	GC
22	12 : 19 : 22.54	+05 : 50 : 17.00	5.75 $\pm$ 1.46	7.54	GCC
23	12 : 19 : 22.67	+05 : 47 : 23.04	3.69 $\pm$ 1.17	4.84	...
24	12 : 19 : 22.81	+05 : 46 : 44.62	3.45 $\pm$ 1.12	4.52	...
25	12 : 19 : 22.99	+05 : 51 : 11.50	1.60 $\pm$ 0.79	2.10	...
26	12 : 19 : 23.00	+05 : 50 : 58.55	5.53 $\pm$ 1.41	7.25	...
27	12 : 19 : 23.10	+05 : 47 : 41.43	7.16 $\pm$ 1.66	9.38	VCC 344
28	12 : 19 : 23.20	+05 : 48 : 07.16	2.69 $\pm$ 0.10	3.53	...
29	12 : 19 : 23.21	+05 : 49 : 29.76	1249.41 $\pm$ 21.02	1638.28	AGN
30	12 : 19 : 23.23	+05 : 50 : 13.44	3.44 $\pm$ 1.12	4.51	GCC
31	12 : 19 : 23.50	+05 : 49 : 36.06	11.02 $\pm$ 4.07	14.45	?
32	12 : 19 : 23.61	+05 : 47 : 55.54	4.70 $\pm$ 1.32	6.16	GC
33	12 : 19 : 24.01	+05 : 49 : 26.42	9.92 $\pm$ 3.02	13.00	?
34	12 : 19 : 24.25	+05 : 47 : 54.75	5.92 $\pm$ 1.50	7.76	...
35	12 : 19 : 24.60	+05 : 51 : 04.86	8.18 $\pm$ 1.73	10.73	GCC
36	12 : 19 : 24.80	+05 : 50 : 57.37	2.40 $\pm$ 0.94	3.15	...
37*	12 : 19 : 24.83	+05 : 50 : 08.61	3.69 $\pm$ 1.17	4.84	GC
38	12 : 19 : 24.93	+05 : 49 : 32.11	5.50 $\pm$ 1.41	7.22	GC
39	12 : 19 : 25.50	+05 : 47 : 41.85	6.53 $\pm$ 1.54	8.57	GCC
40	12 : 19 : 25.55	+05 : 49 : 46.17	4.92 $\pm$ 1.41	6.45	GC
41*	12 : 19 : 25.65	+05 : 50 : 28.75	2.73 $\pm$ 1.06	3.58	GC
42	12 : 19 : 25.95	+05 : 52 : 20.50	3.96 $\pm$ 1.22	5.19	...
43*	12 : 19 : 26.06	+05 : 50 : 13.69	2.76 $\pm$ 0.10	3.62	galaxy
44	12 : 19 : 26.89	+05 : 50 : 44.15	5.74 $\pm$ 1.46	7.52	GC
45	12 : 19 : 29.22	+05 : 50 : 00.59	2.91 $\pm$ 1.06	3.82	GCC
46	12 : 19 : 29.78	+05 : 51 : 14.35	7.46 $\pm$ 1.66	9.78	...
47	12 : 19 : 29.97	+05 : 50 : 28.20	5.64 $\pm$ 1.46	7.39	...
48	12 : 19 : 30.51	+05 : 50 : 07.97	3.11 $\pm$ 1.06	4.08	...
49	12 : 19 : 31.08	+05 : 50 : 07.96	2.50 $\pm$ 0.10	3.28	GCC
50	12 : 19 : 31.98	+05 : 51 : 54.46	5.60 $\pm$ 1.46	7.35	GCC
51	12 : 19 : 32.08	+05 : 51 : 49.47	4.85 $\pm$ 1.41	6.35	...
52	12 : 19 : 33.93	+05 : 50 : 35.75	5.65 $\pm$ 1.46	7.41	...
53	12 : 19 : 35.52	+05 : 50 : 48.93	4.04 $\pm$ 1.27	5.30	NGC 4264
54	12 : 19 : 36.87	+05 : 51 : 56.22	4.44 $\pm$ 1.32	5.82	...

This figure "f1.jpg" is available in "jpg" format from:

<http://arxiv.org/ps/astro-ph/0508189v1>

This figure "f2.jpg" is available in "jpg" format from:

<http://arxiv.org/ps/astro-ph/0508189v1>

This figure "f3.jpg" is available in "jpg" format from:

<http://arxiv.org/ps/astro-ph/0508189v1>

This figure "f4a.jpg" is available in "jpg" format from:

<http://arxiv.org/ps/astro-ph/0508189v1>

This figure "f4b.jpg" is available in "jpg" format from:

<http://arxiv.org/ps/astro-ph/0508189v1>

This figure "f5.jpg" is available in "jpg" format from:

<http://arxiv.org/ps/astro-ph/0508189v1>

This figure "f6.jpg" is available in "jpg" format from:

<http://arxiv.org/ps/astro-ph/0508189v1>

This figure "f7.jpg" is available in "jpg" format from:

<http://arxiv.org/ps/astro-ph/0508189v1>

This figure "f8.jpg" is available in "jpg" format from:

<http://arxiv.org/ps/astro-ph/0508189v1>

This figure "f9a.jpg" is available in "jpg" format from:

<http://arxiv.org/ps/astro-ph/0508189v1>

This figure "f9b.jpg" is available in "jpg" format from:

<http://arxiv.org/ps/astro-ph/0508189v1>